

Article

Analysis of Factors Influencing Mining Damage Based on Engineering Detection and Machine Learning

Lintian Miao ^{1,2,*}, Zhonghui Duan ², Yucheng Xia ¹, Rongjun Du ¹, Tingting Lv ² and Xueyang Sun ¹

¹ College of Geology and Environment, Xi'an University of Science and Technology, Xi'an 710054, China

² Key Laboratory of Coal Resources Exploration and Comprehensive Utilization, Ministry of Natural Resources, Xi'an 710021, China

* Correspondence: mlt@mdpi.com; Tel.: +86-132-2809-6981

Abstract: The direct results of mining damage are overburden fracture and surface subsidence, which may induce groundwater seepage and surface vegetation degradation. Therefore, it is essential to research the factors and mechanisms influencing mining damage. Based on the geological characteristics of the Xiaobaodang minefield in the Yushen Mine area in China, the engineering detection of fractured zone height (FZH), sampling tests of rock mechanical properties, and field measurements of the surface settlement were carried out. Firstly, the factors influencing the FZH were screened by correlation analysis and partial correlation analysis. Next, a model for predicting the maximum height of the fracture zone with the BP neural network (BPNN) was established and trained with Python. Finally, the FLAC^{3D} numerical simulation experiment was adopted to reveal the variation law of overburden stress during coal mining, and the relationship between stress and overburden fracture was analyzed. The results show the following: When the average mining thickness in the study area is 5.8 m, the maximum height of the fractured zone is 157.46 m, and the maximum surface subsidence is 3715 mm. Further, the mining thickness, mining depth, the compressive strength of overburden, the width of the working face, and the mining velocity are the main factors affecting the maximum height of the fractured zone. Additionally, the goodness of fit of the BPNN model can reach 97.22%, meaning that it can effectively predict the maximum height of the fractured zone caused by coal mining. Finally, the area where the stress changes markedly above the goaf is the area where the fractures develop rapidly. Meanwhile, there is a positive correlation between the surface subsidence and the FZH. The research results obtained provide new ideas for reducing mining damage and will be helpful for the green and sustainable development of the mine.

Keywords: mining damage; fractured zone height (FZH); surface subsidence; BP neural network (BPNN); FLAC^{3D}



Citation: Miao, L.; Duan, Z.; Xia, Y.; Du, R.; Lv, T.; Sun, X. Analysis of Factors Influencing Mining Damage Based on Engineering Detection and Machine Learning. *Sustainability* **2022**, *14*, 9622. <https://doi.org/10.3390/su14159622>

Academic Editors: Miao Chen, Yanhua Huang and Yuanchao Zhang

Received: 15 July 2022

Accepted: 1 August 2022

Published: 4 August 2022

Publisher's Note: MDPI stays neutral with regard to jurisdictional claims in published maps and institutional affiliations.



Copyright: © 2022 by the authors. Licensee MDPI, Basel, Switzerland. This article is an open access article distributed under the terms and conditions of the Creative Commons Attribution (CC BY) license (<https://creativecommons.org/licenses/by/4.0/>).

1. Introduction

Coal is an indispensable energy resource for sustainable human existence and economic development [1]. However, coal mining damages the geological and ecological environment of the mining area [2,3]. Direct manifestations of mining damage are overburden fracture and surface subsidence if the bedrock thickness is 90 m or more [4]. Cases of mining damage have occurred in most of the world's coal mining areas [5–7]. Long-term production practice and scientific research have confirmed that mining damage is affected by a variety of mining and geological factors [8–10]. Consequently, the question of how to quantitatively study the factors and mechanisms influencing mining damage is very important in order to reduce the damage caused by mining. It is also one of the major issues to be faced in green sustainable development and scientific coal mining. Machine learning technology provides a more reliable technological means for quantitative research and prediction model construction, which is also the main modeling method used in this paper.

For a long time, the scientific problem of mining damage has attracted the attention of many scholars, who have carried out extensive practical and theoretical research on this

topic. The following studies have been carried out on the height prediction of the overlying bedrock fractured zone caused by coal mining. Wang et al. [11] explored the characteristics of movement and breaking in overlying strata using a scale model experiment, and an overlying strata synchronous movement method was established to predict the height of the goaf. Zhu et al. [12] proposed a method to calculate the height of the water-conducting fracture zone based on the plate and shell theory, which provides the basis for the fractured zone height (FZH) prediction in the Jurassic coalfield of Northern Shaanxi. Liu et al. [13] proposed a new detection method for the connecting fractured zone based on isotope tracing, which was verified by a practical case. Tan et al. [14,15] measured the FZH in overburden strata by combining the loss of the drilling fluid method and numerical simulation. The FZH and its development characteristics in the strip mining of a shallow coal seam under a hard roof were studied, and it was found that the FZH increases in steps with the mining width. Wu et al. [16] carried out a fitting regression analysis based on the coal mine measurement data and obtained the calculation formula of FZH. The calculation results were mostly consistent with the measured values. Liu et al. [17] proposed a prediction method for the height of the water-conducting fractured zone based on multiple regression analysis and a geographic information system. Zhang et al. [18] established an empirical formula for FZH using the measured FZH data of 28 boreholes in a Jurassic coalfield in Northwest China, but the geological background of the data generation was different. There have also been studies on mining subsidence. Fan et al. [19,20] studied the distribution of ground cracks in the Yushenfu mining area using remote sensing technology. They found that the ground cracks in the high-intensity mining areas in the loess hilly area were dense and the surface damage was serious. Li et al. [21] used a terrestrial laser scanner to collect data and adopted the Boltzmann function prediction method exponent Knothe time function to establish a mining subsidence prediction model. Chen et al. [22] established a cellular automata model for the evolution of mining subsidence in three-dimensional space, which reflects the process of surface subsidence. Li et al. [23] used the probability integration method to determine the prediction parameters. They obtained a subsidence function model of the settlement point in overburden, which could dynamically predict the movement and deformation in the overburden. Gong et al. [24] compared the geological conditions and surface subsidence data of 16 coal mines in Western China and established a carefully calibrated numerical model. In addition, Huang et al. [25] adopted a combination of physical simulation experiments and field measurements to research, in depth, the development law and mechanism of surface subsidence caused by the shallow coal seam mining in the Jurassic coal field in northern Shaanxi Province. They found that multi-seam coal pillars are the main factor controlling the surface and overlying bedrock cracks. Chen et al. [26,27] carried out numerical compression simulations on a rock specimen containing non-persistent joints under confining pressure with the bonded-particle model, and obtained the conclusion that both the compressive strength and elastic modulus of the specimens increase with increasing confining pressure. The fruitful research results of these predecessors provided the theoretical basis and data collection technology used in this paper, but they predominantly focused on prediction methods and models. The factors influencing the maximum FZH, as well as the internal relationship between rock strata fractures and surface subsidence, need to be further researched.

In this paper, the research background concerns the 112201 working face of Xiaobao-dang No. 1 coal mine in the Yushen mining area of China, adopting a combination of engineering detection, BPNN, and numerical simulation experiment methods to research the factors influencing FZH and surface deformation above the goaf. The BPNN prediction model of the maximum height of the fracture zone and its influencing factors are given. It is found that the FZH is positively correlated with the amplitude of surface subsidence. Our results are expected to provide a theoretical basis for reducing the damage caused by mining and aiding the construction of green mining areas, which will be conducive to the harmonious development of man and nature.

2. Study Area

The Xiaobaodang minefield is located in the Yushen mining area of the Jurassic coalfield in northern Shaanxi in China, which includes the No. 1 coal mine and mine No. 2 coal mine with an area of 219.64 km². The 2⁻² coal seam is distributed throughout the whole area and is the main workable coal seam in the upper part, as shown in Figure 1. The strata in the area from old to new are as follows: Upper Triassic Yongping Formation (T_{3y}), Middle Jurassic Yan'an Formation (J_{2y}), Zhiluo Formation (J_{2z}), Anding Formation (J_{2a}), Neogene Pliocene Baode Formation (N_{2b}), Quaternary Upper Pleistocene Salawusu Formation (Q_{3s}), and Quaternary Holocene Aeolian sand (Q_{4^{eol}}), according to the borehole exposure and geological mapping data. There are nine coal seams in the Yan'an Formation in the Xiaobaodang minefield. The 2⁻² coal seam is being mined, and the mining method of full mining height has been adopted for the working face. The thickness of the 2⁻² coal seam is 1.06–9.86 m, and the buried depth is 199.69–401.22 m. The thickness of the overlying bedrock 2⁻² of the coal seam is 149.46–359.03 m. The spatial relationship between the coal seam and the stratum is shown in Figure 2.

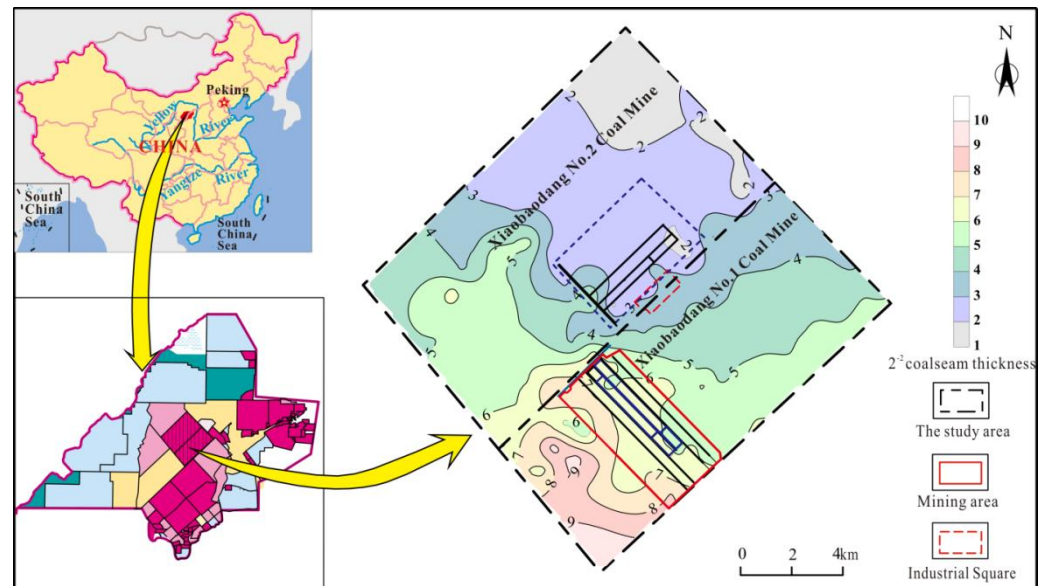


Figure 1. Location and general map situation of Xiaobaodang minefield.

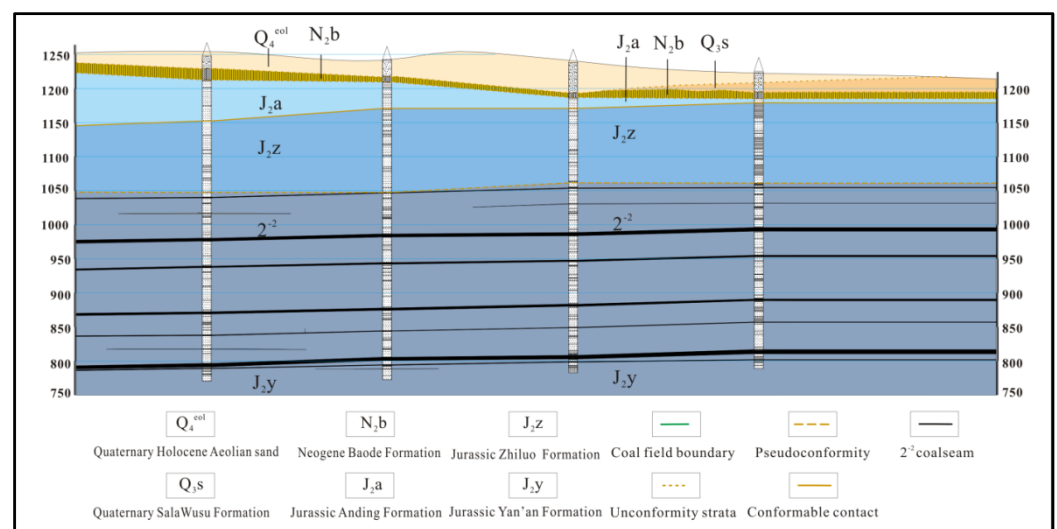


Figure 2. Stratigraphic profile of Xiaobaodang minefield.

The working face 112201 of the Xiaobaodang No. 1 Coal Mine has a strike length of 4660 m, a dip direction length (working face width) of 350 m, and an area of 1.63 km². This working face has been mined, and the uneven subsidence of the surface and overburden fractures have occurred due to coal mining. Further, FZH has been detected, and the surface subsidence is being monitored.

3. Methods

3.1. Detection Method of FZH

In general, it takes at least 3 months for the deformation of the overlying strata to stabilize after coal mining. In order to fully develop the caved zone, the fractured zone, and the curved subsidence zone, all boreholes used to detect the FZH were created 4–8 months after coal mining. There are few detected boreholes in the fractured zone in the Xiaobaodang minefield, so this paper used the detection data of the surrounding minefield in the research process, as the surrounding minefield and the Xiaobaodang minefield have the same geological background, coal seam occurrence characteristics, and mining technology.

Four kinds of engineering techniques are used to detect the FZH, such as the loss of drilling fluid method, the engineering geological catalog, geophysical logging, and image logging. However, not all methods can collect reliable data due to the geological characteristics of the area and borehole stability.

(1) The Loss of Drilling Fluid Method

The main content of the loss of drilling fluid method is the observation of flushing fluid consumption, the mud level, and the drilling tool footage during drilling. If drilling takes place in normal strata, the consumption of the flushing fluid and the water level in the borehole will be very steady. If cracks occur in the rock strata, the consumption of the flushing fluid will increase abruptly, and the water level of the drilling mud will disappear or decline rapidly. There can be differences because of the lithology of the critical surface, the fracture development, and the connection degree.

(2) Core Engineering Geology Catalogue

The main purpose of a core engineering geological catalog is to describe the integrity and the fracture development of the core and to count the RQD value of the core quality index. If the fracture zone or caving zone is entered, the core generally has the following characteristics:

① There will be a significant number of fresh vertical or oblique fracture cracks in the core, ② the core integrity decreases, and the RQD value decreases, and ③ the integrity degree of the core decreases sharply when drilling into the top interface of the caving zone. At this time, the core will become very broken, and the RQD of the core can even reach close to zero. The fracturing of the core will be increased in the longitudinal and oblique directions, and the bedding and dip angle of the core will be disordered.

The engineering geological characteristics of a normal core and a fractured core in the XSD7 borehole obtained by this drilling are shown in Figure 3.

(3) Image Logging

A 360° digital image of the borehole wall is formed by using borehole intelligent panoramic imaging logging, and the top interface of the fractured zone is determined by identifying the development of fractures in the strata through the image. If the fractures increase significantly and there are vertical fractures, this is judged to be the top boundary of the fractured zone. When there is a hole in the strata or deformation in the rock layer, the rock will become extremely broken and is considered to be the top of the caving zone. The fracture development in the XSD7 hole is shown in Figure 4.



Figure 3. Core of borehole XSD7. (a) Normal core; (b) Fractured zone core.

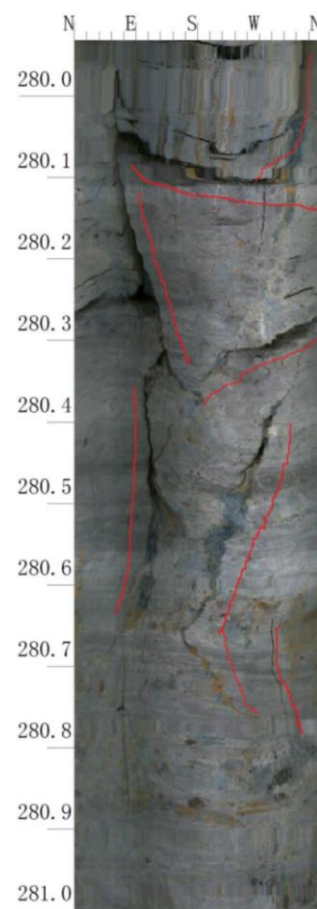


Figure 4. Image logging graph of borehole XSD7.

(4) Geophysical Logging

Lateral resistivity, density, long-source-distance gamma, and short-source-distance gamma are used for comprehensive interpretation. Due to the mining damage, fractures develop in the overburden, and the resistivity and rock mass density decrease sequentially. Therefore, this method is used to explain the fracture development of the borehole wall in order to determine the top interface of the fractured zone. The geophysical logging of the Y6 borehole is shown in Figure 5. Here, the two dashed lines indicate that four geophysical logging curves and flushing fluid leakage curves reflect the top interface of the fracture zone at the same depth.

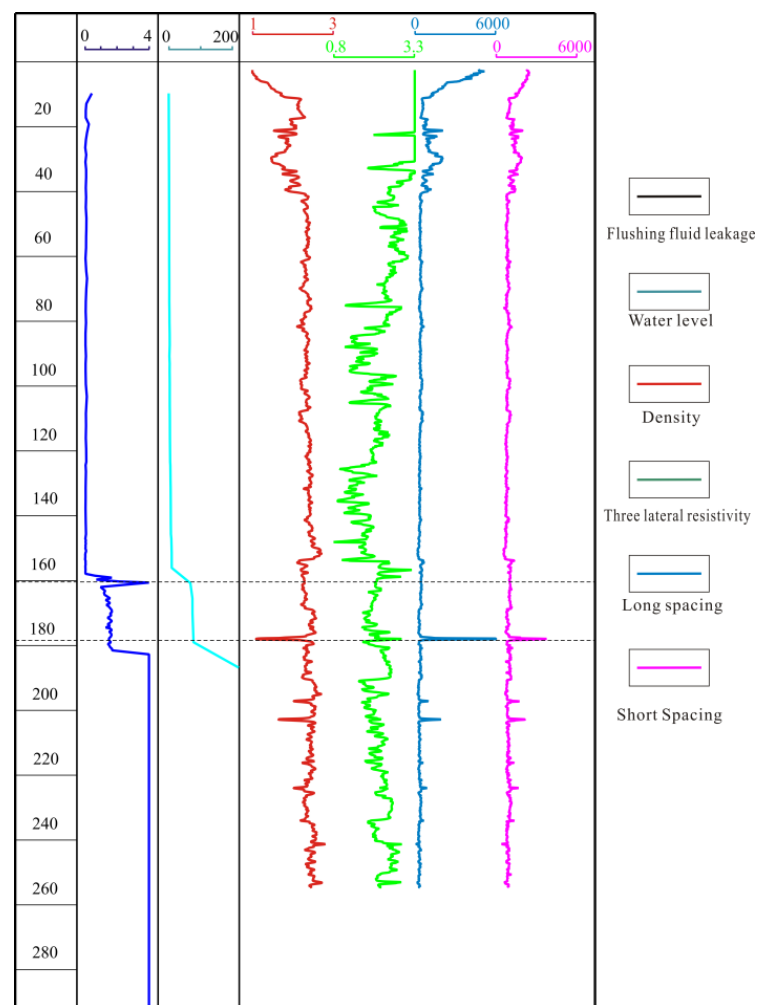


Figure 5. Geophysical logging curves of borehole Y6.

Data collected using the above detection method are shown in Table 1.

Table 1. Field detected data for FZH.

Borehole Number	Determination Data of Loss of Drilling Fluid Method	Determination Data of Geophysical Logging	Determination Data of Engineering Geological Catalogue	Determination Data of Image Logging	Average Fractured Zone Height
Y3	130.5	127.7	127.72	/	128.64
Y4	137.3	136.9	140.8	/	138.33
Y5	138.9	129.2	135.4	/	134.50
Y6	117.8	118.24	118.6	118.5	118.29
H3	108.32	85.53	110.88	108.98	109.39
H4	114.38	136.23	114.18	113.58	114.05
H5	107.83	135.5	108.9	109.9	108.88
ZP1	96.3	/	/	/	96.3
ZP2	84.8	/	/	/	84.8
DZ1	136.52	139.61	133.8	136.1	136.51
DZ2	126.28	128.75	136.4	139.15	132.65
XSD1	158.159	158.909	158.779	154.009	157.46
XSD7	146	155	157.39	156.7	156.36
XSD2	157.083	153.463	153.263	152.013	153.96
JT4	126.4	133.45	127.9	130.7	129.61
JT6	120.25	109.9	118.3	119	119.18

3.2. Surface Settlement Monitoring

3.2.1. Design of Strike Monitoring Line

(1) Position of Strike Monitoring Line

The coal seam of the 112201 working face is near horizontal, and the influence of the inclination angle is not considered. Therefore, a strike monitoring line is laid on the central line of the advancing direction of the working face.

(2) Length of Strike Monitoring Line

The strike monitoring line must cover the radius of the subsidence basin and have a safe distance. The strike length of the working face is 4660 m ($4660 \text{ m} > 1.4H_0$). The strike direction can be fully mined. Therefore, the minimum length of the strike monitoring line is as follows.

$$S_1 \geq 0.7H_0 + (H_0 - h) \cot(\delta - \Delta\delta) + h \cot \varphi \quad (1)$$

where H_0 is the average mining depth of the working face, $H_0 = 302 \text{ m}$;

h is the thickness of the loose layer, $h = 89 \text{ m}$;

φ is the loose layer moving angle, $\varphi = 45^\circ$;

δ is the angle of strike displacement, $\delta = 73^\circ$;

$\Delta\delta$ is the correction value of the moving angle, $\Delta\delta = 20^\circ$.

The minimum length of the strike monitoring line is calculated as $S_1 = 461 \text{ m}$.

As the loose layer of the 112201 working face is thick, in order to ensure that the strike line covers the radius of the subsidence basin, the strike line length is finally determined to be 900 m. A total of 300 m is laid outside the cut-hole mining boundary, and 600 m is laid inside the cut-hole. In total, 37 monitoring points are arranged along the strike monitoring line. The monitoring points are numbered Z01, Z02, Z03 ..., and Z37 and are 25 m apart, as shown in Figure 6.

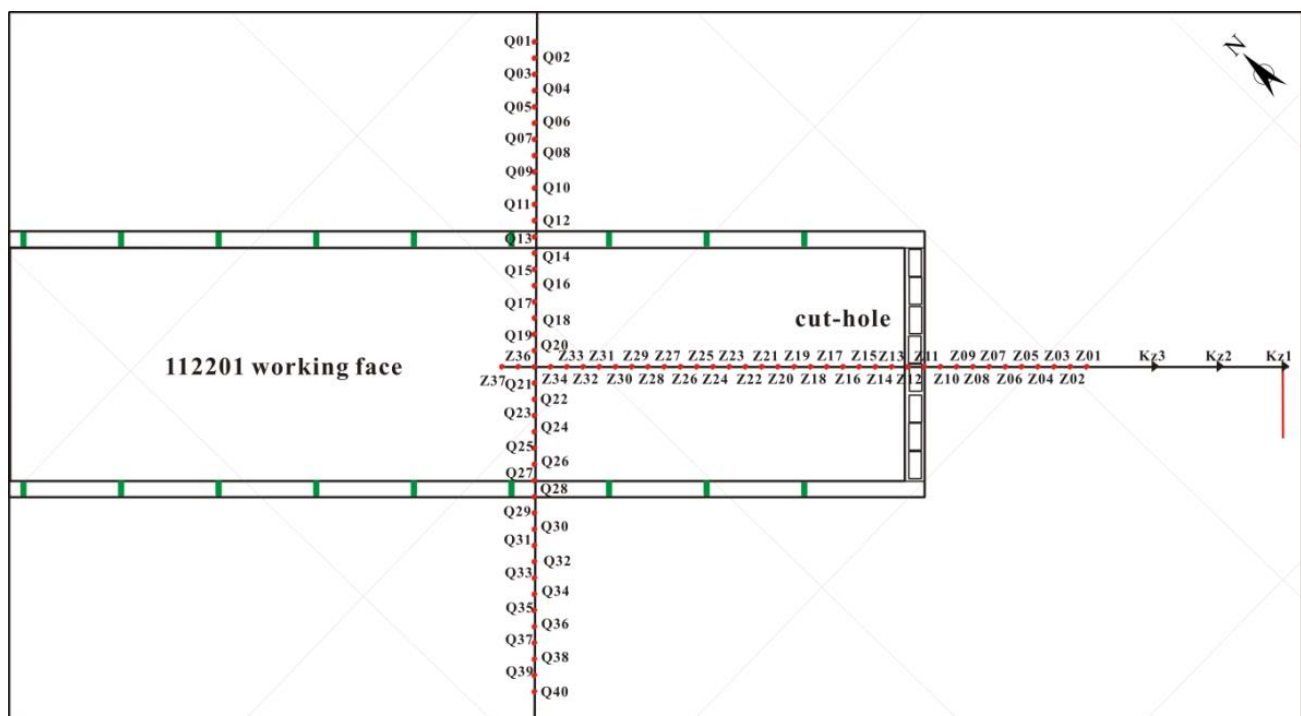


Figure 6. Layout map of the surface monitoring points on 112201 working face in Xiaobaodang No. 1 coal mine.

3.2.2. Design of Dip Monitoring Line

(1) Position of Dip Monitoring Line

The dip monitoring line should be arranged at the maximum subsidence position, and the distance (D) from the dip monitoring line to the cut-hole should conform to Formula (2).

$$D \geq 0.7H_0 \quad (2)$$

where H_0 is the average mining depth of the working face, $H_0 = 302$ m;

According to the calculation results, only when the distance between the dip monitoring line and the cut-hole is greater than 211 m can it be placed in the main section. In order to fully ensure that the dip monitoring line covers the subsidence basin, the dip observation line is arranged 550 m away from the cut-hole. At the same time, the dip observation line intersects vertically with the strike monitoring line at Z35, ensuring that there are two strike line points outside the dip line, as shown in Figure 6.

(2) Length of Dip Monitoring Line

The length of the dip monitoring line must cover the width of the subsidence basin and the working face and have a certain safe distance. The dip length of the working face $L = 350$ m ($350 \text{ m} < 1.4H_0$)—that is, the dip direction may not reach full mining. The minimum length of the dip monitoring line is as follows:

$$S_2 \geq 2(H_0 - h) \cot(\delta - \Delta\delta) + 2h \cot \varphi + l \quad (3)$$

The letters have the same meanings as the letters in Formula (1).

The minimum length of the dip observation line S_2 can be obtained from the equation $S_2 = 849$ m.

As the loose layer of the 112201 working face is thick, the length of the dip monitoring line is set to 1000 m to ensure that the subsidence basin is covered and the monitoring needs are met. In total, 40 monitoring points were arranged at a distance of 25 m. The numbering sequence of the monitoring sites is Q01, Q02, Q03 . . . , and Q40, as shown in Figure 6.

3.3. Test Method of Rock Mechanics Parameters

In order to discover the mechanical properties of the overlying strata of the coal seam, we followed the *Methods for determining the Physical and Mechanical Properties of Coal and Rock (GB/T 23561-2009)* for the determination of uniaxial saturation compressive strength (USCS) and the calculation of the softening coefficient, as shown in Figure 7. The test data are shown in Table 2.

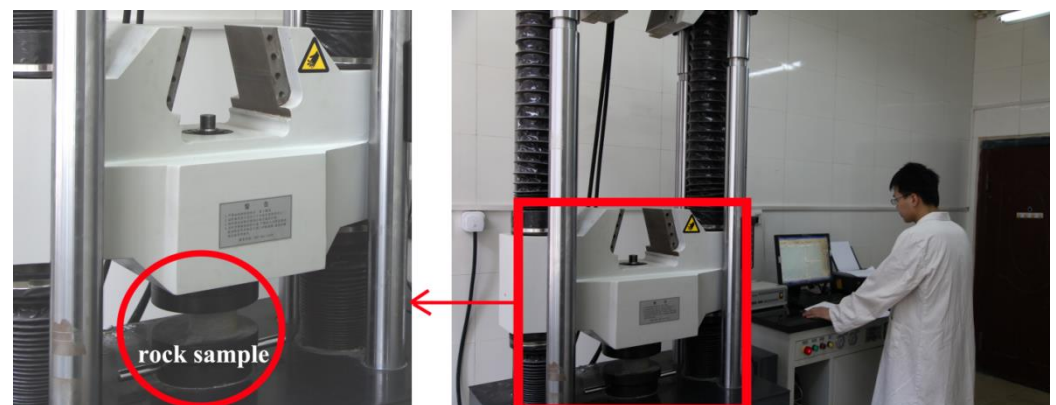


Figure 7. Rock mechanics parameter testing.

Table 2. Rock mechanical parameter of Xiaobaodang minefield.

Strata	Drilling Number	Rock Name	Sampling Depth (M)	USCS (Mpa)	Softening Coefficient	Poisson's Ratio
J2z	BK2	Siltstone	126~145.97	18.8	0.77	0.23
		Medium Grained Sandstone	145.97~156.83	18.32	0.84	0.22
		Siltstone	156.83~166.93	16.33	0.62	0.23
		Fine-Sandstone	166.93~175.27	18.48	0.7	0.23
		Coarse Sandstone	175.27~185.4	11.19	0.78	0.21
		Siltstone	185.4~195.3	11.99	0.49	0.23
		Coarse Sandstone	195.3~209.1	12.57	0.61	0.22
	3#	Sandy Mudstone	146.10~150.25	0.836	0.04	0.37
	9#	Sandy Mudstone	106.58~121.19	8.18	0.21	0.3
	10#	Sandy Mudstone	173.6~176.36	0.618	0.03	0.35
	11#	Sandy Mudstone	235.10~242.73	21.6	0.6	0.27
		Sandy Mudstone	282.3~289.41	18.2	0.57	0.28
J2y	BK2	Siltstone	209.1~212.6	15.63	0.79	0.22
		Fine-Sandstone	212.6~216.5	17.1	0.81	0.22
		Coarse Sandstone	216.5~223.5	13.97	0.7	0.22
		Siltstone	224.15~229.5		0	0.23
		Medium Grained Sandstone	229.5~237.47	16.9	0.71	0.22
		Siltstone	237.47~240.97	12.53	0.54	0.22
		Siltstone	244.9~251.81	15.77	0.71	0.22
		Fine-Sandstone	251.85~253.45	19.27	0.82	0.23
		Siltstone	253.45~261.55	23.01	0.79	0.23
		Coarse Sandstone	261.55~263.85	16.51	0.76	0.22
		Siltstone	263.85~267.51	26.28	0.81	0.24
		Coarse Sandstone	267.51~271.51	16.82	0.78	0.22
		Siltstone	271.51~284.08	17.18	0.57	0.23
		Coarse Sandstone	284.08~290.1	12.55	0.38	0.24
		Fine-Sandstone	292.08~296.12	21.3	0.78	0.23
		Coal	296.8~302.7	14.86	0.69	0.22

3.4. Machine Learning Modeling of FZH Prediction

3.4.1. Feature Dimension Reduction Method

The geological and mining factors affecting FZH were determined, and the other irrelevant or weakly correlated factors were eliminated. Correlation analysis is not only an effective method for eliminating irrelevant factors but also an important method for feature dimension reduction in machine learning [28]. In this paper, a Pearson correlation analysis was used to calculate the Pearson correlation coefficient r and significance parameter p between all indexes and the FZH, based on the data obtained from the engineering detection and sampling test, where $r < 0$ means negative correlation; $r > 0$ indicates positive correlation; and the bigger $|r|$ is, the greater the relevance is. If $|r| > 0.5$ and $p < 0.05$, the corresponding factors are judged to be in significant correlation with FZH, while $p > 0.05$ and $|r| < 0.5$ indicate that the factors have been abandoned [29]. According to the geological theory and the Pearson correlation analysis results, the autocorrelation between retention factors was calculated, and a partial correlation analysis was conducted. The factors with $p > 0.05$ were excluded under the control variables.

3.4.2. The Modeling Method

After feature dimension reduction, there are five features (independent variables) and only one label (dependent variables—FZH) to be predicted in this problem, which is a continuous variable. The essence of this problem is to study how five features jointly determine one label. This is a typical case of supervised learning. An artificial neural network has unique advantages in solving this problem. An artificial neural network can update the weights of different input parameters in the hidden layer through continuous self-iteration, meaning that the regression accuracy of the model as a whole can reach the optimal point. This approach is often used to model complex relationships between inputs and outputs.

BPNN is currently one of the most widely used neural network models. It is a multilayer feed-forward network with error backpropagation training, and its algorithm is called the BP algorithm. In essence, the BP algorithm takes the network error square as an objective function and uses the gradient descent method to calculate the minimum value of the objective function. Structurally, BPNN has an input layer, a hidden layer, and an output layer. BPNN has an arbitrarily complex pattern classification ability and an excellent multi-dimensional function mapping ability. Many studies [30,31] have elaborated the mathematical principle of BPNN, which will not be repeated here. A three-layered BPNN is used in this paper to construct the prediction model of FZH. The modeling method is as follows: ① A data set is generated from the data obtained by engineering exploration, ② a correlation analysis and partial correlation analysis are used to reduce the dimensions of the data set, ③ the data set is divided into a training set and a test set, ④ we design and build the BPNN model, ⑤ we input the training set and train the model by adjusting the number of hidden layer neurons, and ⑥ we input the test set to evaluate the BPNN model. The modeling process is shown in Figure 8. The mean square error (MSE) and the coefficient of determination (R^2) are usually used to evaluate the degree of model fitting. The calculation formula is as follows:

$$MSE = \frac{1}{n} \sum_{i=1}^n (y_i - \hat{y}_i)^2 \quad (4)$$

$$R^2 = \frac{\sum_{i=1}^n (\hat{y}_i - \bar{y})^2}{\sum_{i=1}^n (y_i - \bar{y})^2} \quad (5)$$

where y_i is the actual measured value;

\hat{y}_i is a fitted value;

\bar{y} is the average of the actual measured value.

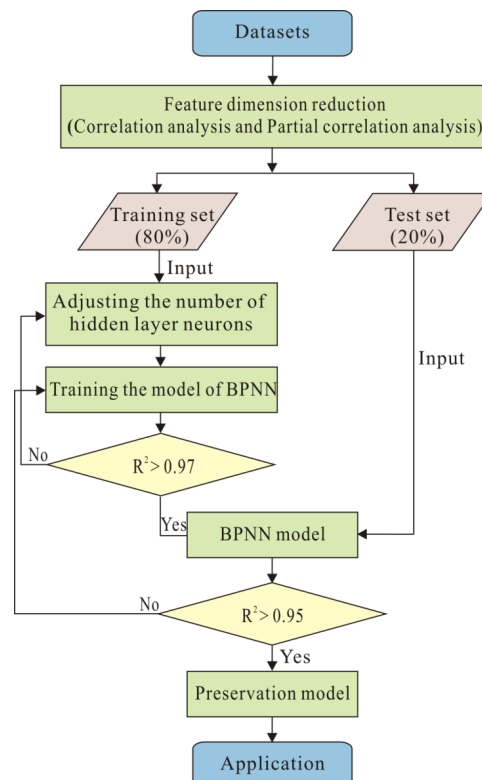


Figure 8. The flow chart of the modeling.

3.5. Numerical Subsidence Experiment

3.5.1. Numerical Model Design and Modeling

FLAC^{3D} has been widely used in mining damage simulation. The finite difference method has been used to establish the calculation equations of the element stress–strain and node displacement [32]. The software can help to build large-scale complex numerical simulations under the conditions of small memory, high precision, and fast operation speed. The advantage of the use of this software in mining engineering is that it takes the motion equation as the basic difference equation and can simulate the dynamic process of the material and structure gradually stabilizing, then undergoing plastic failure, before finally gradually stabilizing. This is close to the stability of a rock mass affected by mining in mining engineering. However, not all of the numerical results are consistent with those of the corresponding physical experiments. FLAC^{3D} has certain advantages in simulating the rock and soil mass deformation, which can well reflect the rock fracture type and the surface settlement amplitude, but it is inferior in simulating the time relationship between coal mining and the surface settlement.

Based on the formation parameters of hole 52-2 in the 112201 working face, the FLAC^{3D} model was designed to simulate the mining damage characteristics of the 112201 working face. The results are shown in Table 3. The numerical model consists of 35 layers of coal and rock strata. The thickness of the simulated 2^{−2} coal seam mining is 6 m, and the thickness of the underlying rock and soil layer is 327 m.

Table 3. The mechanical parameters of rock in the numerical experimental model.

Lithology	Thickness (m)	Elastic Modulus ($\times 10^4$ Mpa)	Tensile Strength (Mpa)	Volumetric Weight (kg/m ³)	Internal Friction Angle (°)	Poisson Ratio	Bond (Mpa)
Soil Layer	12	0.168	0.20	2710	39.7	0.57	0.83
Silty Clay	70	0.503	0.16	2720	43.5	0.49	0.85
Siltstone	2	0.854	0.42	2420	38.66	0.22	0.85
Medium-Grained Sandstone	4	0.452	0.24	2310	39.55	0.18	0.51
Siltstone	15	1.325	0.75	2390	38.58	0.21	1.42
Fine-Grained Sandstone	9	1.195	0.68	2310	38.66	0.23	1.26
Medium-Grained Sandstone	6	0.563	0.32	2350	40.22	0.18	0.51
Siltstone	8	1.795	0.95	2430	37.69	0.21	1.83
Fine-Grained Sandstone	2	1.598	0.81	2340	38.25	0.2	1.62
Siltstone	6	1.425	0.73	2470	37.45	0.21	1.52
Fine-Grained Sandstone	4	1.421	0.71	2350	38.66	0.2	1.52
Medium-Grained Sandstone	6	1.328	0.72	2320	38.66	0.2	1.41
Coarse-Grained Sandstone	5	1.214	0.63	2310	41.8	0.19	1.28
Fine-Grained Sandstone	12	1.758	0.97	2360	35	0.23	1.82
Siltstone	17	2.214	1.17	2390	38.77	0.19	2.38
Fine-Grained Sandstone	3	2.318	1.22	2350	39.55	0.23	2.42
Medium-Grained Sandstone	14	2.425	1.35	2330	39.08	0.15	2.63
Siltstone	15	2.758	1.41	2310	37.43	0.19	2.85
Fine-Grained Sandstone	6	1.425	0.71	2350	38.66	0.2	1.51
Siltstone	11	1.385	0.78	2410	36.27	0.23	1.59
Fine-Grained Sandstone	10	1.427	0.71	2380	38.19	0.24	1.54
Medium-Grained Sandstone	14	2.458	1.32	2410	37.75	0.22	2.65
Siltstone	4	1.569	0.85	2420	38.26	0.18	1.75
Medium-Grained Sandstone	9	2.587	1.36	2380	36.03	0.15	2.74
Siltstone	3	1.325	0.73	2460	38.47	0.2	1.42
Fine-Grained Sandstone	2	2.658	1.31	2370	37.43	0.15	2.71
Siltstone	5	2.412	1.17	2410	36.3	0.17	2.49
Fine-Grained Sandstone	5	2.758	1.45	2320	38.05	0.15	2.86
Medium-Grained Sandstone	2	2.153	1.14	2360	39.45	0.2	2.24
Fine-Grained Sandstone	5	2.745	1.47	2380	38.66	0.17	2.86
Siltstone	7	2.135	1.15	2350	39.78	0.22	2.26
Medium-Grained Sandstone	32	1.247	0.67	2280	37.69	0.16	1.3
Siltstone	2	2.658	1.46	2380	38.65	0.2	2.8
2 ^{−2} Coal	6	0.658	0.24	1360	38.48	0.17	0.61
Siltstone	58	3.421	1.74	2360	38.66	0.16	3.44

3.5.2. Simulated Excavation and Model Testing

The strike length of the FLAC^{3D} numerical model is 1000 m, and the dip length is 10 m. In order to eliminate the boundary effect, the strike mining length of the model is 800 m, 100 m of coal pillars are left on both sides, and 100 m of coal is mined each time. The model testing methods include the contrast between the measured maximum surface subsidence and the simulated results, as well as the contrast between the measured FZH and the simulated results. In the simulation diagram, the plastic zone represents the area of rock failure. The height of the fracture zone is determined according to the highest position from the roof of the coal seam in the plastic zone. The surface subsidence curves obtained from the numerical simulation experiment are shown in Figure 9. When the working face advanced to 100 m, the surface subsidence was small. When the face advanced to 200 m, the surface subsidence increased rapidly, and the subsidence range expanded obviously. Similarly, when advancing to 300 m and 400 m, both the amount and the range of surface subsidence increased rapidly.

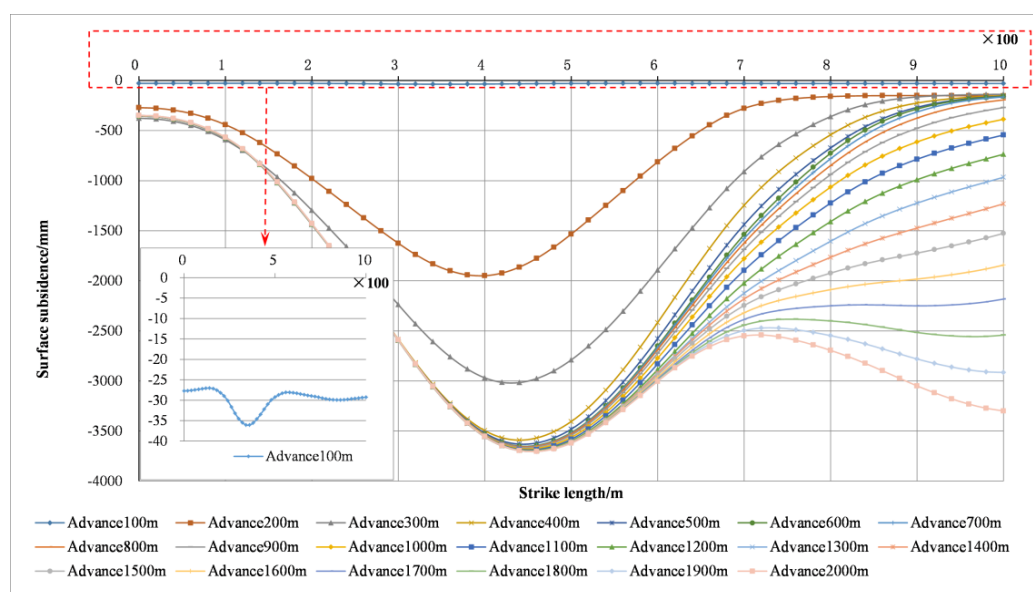


Figure 9. Surface subsidence curve of numerical simulations.

The maximum surface subsidence was extracted from the numerical simulation experiment; the results are shown in Table 4.

Table 4. Comparison between the maximum surface subsidence and FHZ.

Advance Distance/m	Maximum Surface Subsidence/mm	FZH/m	Advance Distance/m	Maximum Surface Subsidence/mm	FZH/m
100	36.16	62.70	500	3630.80	163.90
200	1949.00	98.10	600	3651.50	164.10
300	3020.80	114.10	700	3654.90	164.50
400	3591.00	145.20	800	3658.20	165.10

According to the results measured in the study area, the maximum surface subsidence was 3715 mm. The maximum surface subsidence of the simulated experiment was 3658.20 mm, differing from the measured value by +56.8 mm. It can be seen from the comprehensive comparison that the numerical simulation experiment results were good.

4. Results

4.1. Monitoring Results of Surface Subsidence

It can be seen from Figure 10 that when the working face advanced to 80 m, the subsidence of points Z11–Z18 on the strike line exceeded 10 mm, indicating that the rock movement above the working face affected the surface monitoring points. When the working face was exhausted, the subsidence of each monitoring point of the strike line rapidly decreased and gradually tended to be stable. The maximum subsidence of 3715 mm occurred at point Z18 when the working face advanced to 3300 m.

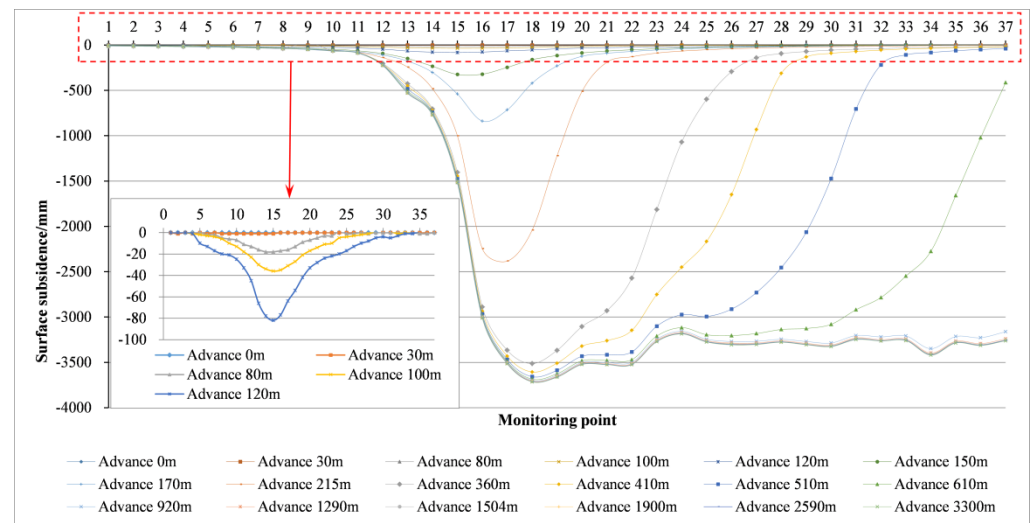


Figure 10. Surface subsidence curve of 112201 working face strike line.

It can be seen from Figure 11 that when the 112201 working face advanced to 360 m, the movement and deformation of the strata above the working face affected points Q11–Q29 on the dip observation line. When the working face advanced to 610 m, just passing directly below the dip observation line, the subsidence amplitude and range of the dip direction rapidly extended. When the working face advanced to 3300 m, the dip observation line lagged far behind the advancing distance of the working face, and the surface movement and deformation moved from weak to strong. At this time, the maximum subsidence of the dip observation line was 3327 mm, which occurred at a point located at Q20.

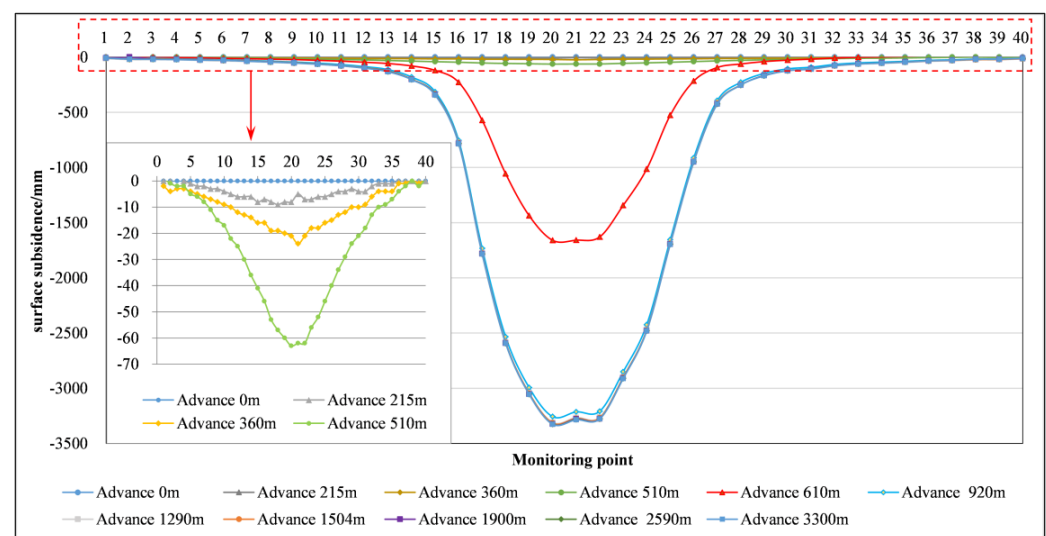


Figure 11. Surface subsidence curve of 112201 working face dip line.

4.2. Weighted Average Value of Rock Mechanical Parameters

By comparing the data measured in the field with the stratum thickness data, it can be seen that the fractured zone only occurred in the Yan'an and Zhiluo formations in the study area. Consequently, only the rock mechanical parameters of the Yan'an and Zhiluo formations were calculated when considering the rock mechanical parameters that affect the FZH.

(1) According to Table 2, the average USCS of various lithologic strata in Zhiluo Formation and Yan'an Formation were obtained, respectively, as shown in Tables 5 and 6.

Table 5. Average USCS of each lithologic strata in Zhiluo Formation.

Lithological	Average USCS
Sandy Mudstone	$\bar{R}_{z1} = (0.836 + 8.18 + 0.618 + 21.6 + 18.2)/5 = 9.89$
Siltstone	$\bar{R}_{z2} = (18.8 + 16.33 + 11.19)/3 = 15.71$
Fine-Grained Sandstone	$\bar{R}_{z3} = 18.48$
Medium-Grained Sandstone	$\bar{R}_{z4} = 18.32$
Coarse-Grained Sandstone	$\bar{R}_{z5} = (11.19 + 12.57)/2 = 11.88$

Table 6. Average USCS of each lithologic stratum in Yan'an Formation.

Lithological	Average USCS
Sandy Mudstone	$\bar{R}_{y1} = x$
Siltstone	$\bar{R}_{y2} = (15.63 + 12.53 + 15.77 + 23.0 + 26.28 + 17.18)/6 = 18.40$
Fine-Grained Sandstone	$\bar{R}_{y3} = (17.1 + 19.27 + 21.3)/3 = 19.22$
Medium-Grained Sandstone	$\bar{R}_{y4} = 16.90$
Coarse-Grained Sandstone	$\bar{R}_{y5} = (13.97 + 16.51 + 16.82 + 12.55)/4 = 14.96$

The average USCS vector of various lithologic stratum in the Yan'an Formation.

$$\bar{R}_z = (\bar{R}_{z1}, \bar{R}_{z2}, \bar{R}_{z3}, \bar{R}_{z4}, \bar{R}_{z5}) = (9.89, 15.71, 18.48, 18.32, 11.88)$$

The average USCS vector of various lithologic strata in the Yan'an Formation.

$$\bar{R}_y = (\bar{R}_{y1}, \bar{R}_{y2}, \bar{R}_{y3}, \bar{R}_{y4}, \bar{R}_{y5}) = (x, 18.40, 19.22, 16.9, 14.96)$$

(2) Taking the data of borehole XSD1 (Table 7) as examples, the cumulative thickness of each lithologic stratum in the Zhiluo Formation and the Yan'an Formation of borehole XSD1 was calculated, respectively.

Table 7. The cumulative thickness of each lithologic stratum of borehole XSD1.

	Sandy Mudstone Thickness (h_1)	Siltstone Thickness (h_2)	Fine-Grained Sandstone Thickness (h_3)	Medium-Grained Sandstone Thickness (h_4)	Coarse-Grained Sandstone Thickness (h_5)	Strata Thickness (H)
J _{2z}	3.58	43.92	17.88	46.01	16.73	128.12
J _{2y}	0	68.44	3.26	0	0	71.7

The cumulative thickness vector of various lithologic stratum in the Zhiluo Formation of borehole XSD1 is shown as follows:

$$H_z = (h_{z1}, h_{z2}, h_{z3}, h_{z4}, h_{z5}) = (3.58, 43.92, 17.88, 46.01, 16.73)$$

The cumulative thickness vector of various lithologic stratum in the Yan'an Formation of borehole XSD1 is shown as follows:

$$H_y = (h_{y1}, h_{y2}, h_{y3}, h_{y4}, h_{y5}) = (0, 68.44, 3.26, 0, 0)$$

(3) The weighted average USCS (\bar{R}) of Yan'an Formation and Zhiluo Formation in the XSD1 borehole was calculated as follows:

$$\begin{aligned}\bar{R} &= \frac{H_z \times (\bar{R}_z)^T + H_y \times (\bar{R}_y)^T}{H} \\ &= \frac{(3.58, 43.92, 17.88, 46.01, 16.73, 128.13) \times (9.89, 15.71, 18.48, 18.32, 11.88)^T + (0, 68.44, 3.26, 0, 0, 71.7) \times (x, 18.40, 19.22, 16.9, 14.96)^T}{128.12 + 71.7} \\ &= 17.11\end{aligned}$$

Similarly, the weighted average USCS of the Yan'an and Zhiluo formations of all boreholes was calculated by the same method. The weighted average of softening coefficient and Poisson's ratio were also calculated by the above method, and the detailed results are shown in Table 8.

Table 8. Actual measured data of the fractured zone and its influencing factors.

Independent Variables									Dependent Variable
Borehole Number	Mining Thickness (M)/M	Mining Depth (S)/M	Overlying Rock Thickness (H1)/M	Working Face Width (W)/M	Mining Velocity (V)/M/D	Weighted Average of USCS of Overburden (\bar{R})/Gpa	Softening Factor (K)	Poisson's Ratio (M)	FZH (H)/m
Y3	5.00	278.50	157.90	255.00	14.99	29.06	0.58	0.44	128.64
Y4	5.00	279.30	160.44	297.00	10.81	29.92	0.56	0.50	138.33
Y5	5.00	286.90	167.70	255.00	8.72	29.52	0.60	0.53	134.50
Y6	5.00	275.80	129.30	255.00	15.00	34.42	0.51	0.23	118.29
H3	4.50	243.48	158.18	300.00	5.29	27.71	0.61	0.35	109.39
H4	4.50	242.18	158.56	300.00	5.29	26.67	0.55	0.34	114.05
H5	4.50	242.90	156.80	300.00	5.29	27.90	0.57	0.34	108.88
ZP1	3.50	208.00	135.00	192.20	4.88	25.30	0.51	0.30	96.30
ZP2	3.50	188.00	120.00	192.20	2.77	26.90	0.53	0.28	84.80
DZ1	6.00	269.80	175.00	350.00	11.30	20.50	0.63	0.22	136.50
DZ2	6.00	273.40	178.90	350.00	10.00	18.75	0.63	0.23	132.65
XSD1	5.80	309.96	214.50	350.00	10.50	17.11	0.49	0.18	157.46
XSD7	5.47	310	239.60	350.00	12.00	21.12	0.70	0.20	156.36
XSD2	5.53	294.61	211.15	350.00	10.50	16.02	0.65	0.23	153.96
JT4	5.50	266.20	215.26	300.00	11.50	25.11	0.58	0.26	129.61
JT6	5.50	265.70	199.80	300.00	11.50	27.36	0.63	0.24	119.18

4.3. Modeling Index Selection

According to the theory of coal mine engineering geology and the practice of coal mining, the FZH is controlled by a variety of mining geological factors [33]. Mining thickness provides a spatial scale for overburden movement, which directly affects the redistribution of stress, deformation, and the rupture range of the roof rock mass. The mining depth has a certain influence on the FZH. Generally, the in situ stress of the surrounding rock increases with the increase in the mining depth. The width of the working face influences the mining space size in the FZH. The mining practice shows that the advancing speed of the working face has an obvious influence on the overburden deformation and failure process [34]. USCS, Poisson's ratio, and the softening coefficient are all mechanical parameters of rock resistance to deformation. The following eight indicators were used as the research objects affecting the FZH, and the data are shown in Table 8.

4.3.1. Feature Dimension Reduction

Correlation analysis was used to obtain the correlation between the eight indicators and the FZH. The correlation coefficient (r) and significance parameter p were calculated using IBM SPSS Statistics 21, and the results are shown in Table 9.

As demonstrated by the Pearson correlation (r) and Sig. (2-tailed) shown in Table 9, it can be concluded that the correlation between the softening coefficient and FZH is not significant, nor is Poisson's ratio. Therefore, these two indexes were eliminated.

Table 9. Correlations ^c.

		Mining Thickness	Mining Depth	Overlying Rock Thickness	Working Face Width	Mining Velocity	Compressive Strength	Softening Factor	Poisson's Ratio
FZH	Pearson Correlation (r)	0.827 **	0.953 **	0.800 **	0.783 **	0.646 **	−0.552 *	0.447	−0.168
	<i>p</i>	0.000	0.000	0.000	0.000	0.007	0.027	0.083	0.533

** Correlation is significant at the 0.01 level (2-tailed). * Correlation is significant at the 0.05 level (2-tailed).

^c. Listwise *N* = 16.

It can be concluded from the results of the Pearson correlation analysis and geological common knowledge that there is a close correlation between the mining depth and the overlying rock thickness. Therefore, the partial correlation analysis method was used to analyze the correlation between the FZH, the mining depth, and the overlying rock thickness. IBM SPSS Statistics 21 was used in the calculation process. The results show that the overlying rock thickness has little effect, and thus it was not considered.

When the overlying rock thickness was used as the control variable, the results of the Pearson correlation analysis were compared with those of the partial correlation analysis. The significance parameter *p* between the FZH and the mining depth was 0.00, the correlation coefficient was 0.953, and the partial correlation coefficient was 0.900, as shown in Table 10a, indicating that there was a strong positive linear correlation between the two variables. This shows that the overlying rock thickness has little effect on the linear correlation between FZH and the mining depth.

Table 10. Results of partial correlation analysis (a). Results of partial correlation analysis (b).

(a)					
Control Variables			FZH	Mining Depth	Overlying Rock Thickness
-none- ^a	FZH	Correlation	1.000	0.953	0.800
		<i>p</i>	-	0.000	0.000
		df	0	14	14
	Mining depth	Correlation	0.953	1.000	0.729
		<i>p</i>	0.000	-	0.001
		df	14	0	14
Overlying rock thickness	Correlation	0.800	0.729	1.000	
	<i>p</i>	0.000	0.001	-	
	df	14	14	0	
Overlying rock thickness	FZH	Correlation	1.000	0.900	
		<i>p</i>	-	0.000	
		df	0	13	
	Mining depth	Correlation	0.900	1.000	
		<i>p</i>	0.000	-	
		df	13	0	
(b)					
Control Variables			FZH	Overlying Rock Thickness	Mining Depth
-none- ^a	FZH	Correlation	1.000	0.800	0.953
		<i>p</i>	-	0.000	0.000
		df	0	14	14
	Overlying rock thickness	Correlation	0.800	1.000	0.729
		<i>p</i>	0.000	-	0.001
		df	14	0	14
Mining depth	Correlation	0.953	0.729	1.000	
	<i>p</i>	0.000	0.001	-	
	df	14	14	0	

Table 10. Cont.

(b)				
Control Variables		FZH	Overlying Rock Thickness	Mining Depth
Mining depth	FZH	Correlation	1.000	0.510
		<i>p</i>	-	0.052
		df	0	13
	Overlying rock thickness	Correlation	0.510	1.000
		<i>p</i>	0.052	-
		df	13	0

^a Cells contain zero-order (Pearson) correlations.

When the mining depth is taken as the control variable, compared with the results of Pearson correlation analysis and partial correlation analysis, the correlation coefficient between the FZH and the overlying rock thickness is 0.800, while their partial correlation coefficient is 0.510. Additionally, the significance parameter *p* was 0.052, which is greater than 0.05, as shown in Table 10b, indicating that there was no obvious linear correlation between them.

In summary, the mining depth has a great effect on the FZH, and the mining depth also has a certain effect on the overlying rock thickness. Therefore, when the mining depth is controlled, the overlying rock thickness has no significant linear effect on the FZH. The overlying rock thickness is excluded.

The following five features are adopted as the influence indexes to study the maximum height of the fractured zone:

M—mining thickness;

S—mining depth;

W—working surface width;

V—mining velocity;

\bar{R} —weighted average of the USCS of overlying rock.

4.3.2. Model Fitting Results

In this paper, we wrote programs in Python. The *MLPRegressor* was called by *neural_network*, a neural network model of the *sklearn* machine learning library, and the BPNN model was established and trained. The activation function used *relu*, the gradient descent method used *adam*, the penalty coefficient was 0.0001, and the number of iterations was less than 20,000. According to the above analysis, five independent variables determine one dependent variable. Thus, there were five neurons in the input layer and one neuron in the output layer. A three-layer neural network model was established. The measured data were imported as the data set. After repetition adjustment and training, when the number of neurons in the hidden layer was 8, the MSE was the smallest, and R^2 was the largest after 2047 iterations. Thus, the topological structure of the BPNN model was 5-8-1. At this point, $i = 5$, $j = 8$, and $k = 1$. The BPNN model training results are presented in Table 11. The weight coefficient matrix is as follows.

$$\omega_{ij} = \begin{bmatrix} 2.1398 \times 10^{-2} & 3.1995 \times 10^{-1} & -1.3265 \times 10^{-1} & 3.5736 \times 10^{-2} & 4.208 \times 10^{-1} & -1.5645 \times 10^{-3} & -3.353 \times 10^{-4} & -4.1047 \times 10^{-1} \\ -2.2287 \times 10^{-2} & 1.7005 \times 10^{-1} & 1.0028 \times 10^{-1} & -3.6130 \times 10^{-1} & 3.7868 \times 10^{-1} & -2.7116 \times 10^{-2} & 2.6923 \times 10^{-49} & 1.5749 \times 10^{-1} \\ -2.2927 \times 10^{-2} & 4.0504 \times 10^{-1} & -4.4932 \times 10^{-2} & 2.4799 \times 10^{-1} & 4.8707 \times 10^{-1} & -2.3800 \times 10^{-2} & 4.5017 \times 10^{-31} & 9.0857 \times 10^{-2} \\ -1.4152 \times 10^{-1} & 2.7234 \times 10^{-1} & -5.2900 \times 10^{-1} & -1.8371 \times 10^{-1} & 2.6498 \times 10^{-1} & 4.9826 \times 10^{-3} & -1.1379 \times 10^{-10} & -3.9350 \times 10^{-1} \\ -2.2184 \times 10^{-2} & 1.3691 \times 10^{-1} & -2.2813 \times 10^{-1} & 1.2475 \times 10^0 & -22.7859 \times 10^{-1} & -1.6898 \times 10^{-2} & -4.3466 \times 10^{-49} & 3.3756 \times 10^{-1} \end{bmatrix}$$

$$\omega_{jk} = [-7.6997 \times 10^{-4} \quad 7.8534 \times 10^{-1} \quad 9.1003 \times 10^{-1} \quad -1.0720 \times 10^0 \quad -2.6198 \times 10^{-1} \quad -2.0059 \times 10^{-2} \quad -6.0434 \times 10^{-4} \quad 8.6912 \times 10^{-1}]^T$$

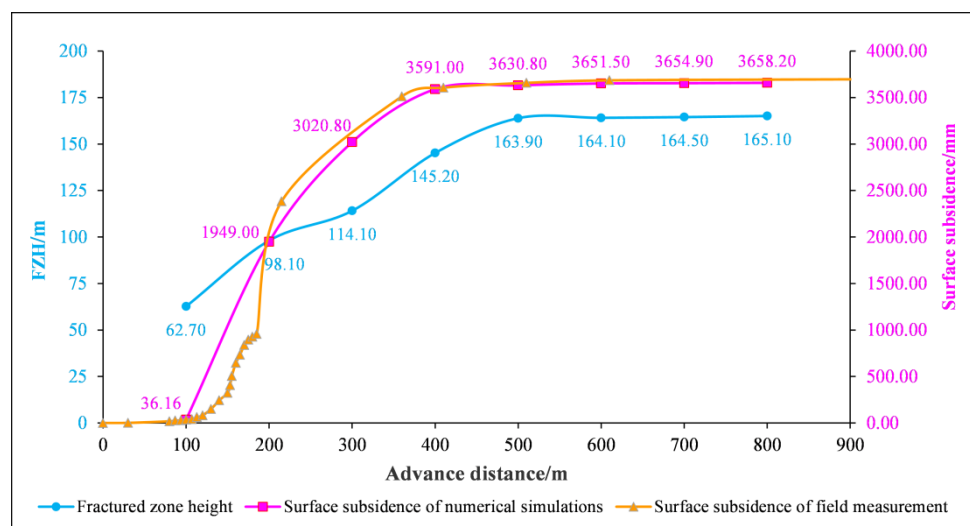
where ω_{ij} is the weight matrix between the input layer and the hidden layer, and ω_{jk} is the weight matrix between the hidden layer and the output layer.

Table 11. The comparison between the predicted results of the BPNN model and the measured results.

Borehole No.	Measured	Fitted	Residual	Role	R ²	MSE
Y3	128.64	128.1314493	0.50855066	training	0.9722	11.1680
Y4	138.33	130.624154	7.70584602	training		
Y5	134.5	134.7158739	−0.21587391	training		
Y6	118.29	123.0760406	−4.78604061	training		
H3	109.39	112.4510121	−3.06101212	training		
H4	114.05	112.7202817	1.32971826	training		
H5	108.88	111.8705876	−2.9905876	training		
ZP1	96.3	96.56931784	−0.26931784	training		
ZP2	84.8	82.87597818	1.92402182	training		
DZ1	136.5	131.9540331	4.54596686	training		
DZ2	132.65	136.7946033	−4.1446033	training		
XSD1	157.46	157.7009284	−0.24092836	training		
XSD7	156.36	157.2740274	−0.91402743	training		
XSD2	153.96	153.3356703	0.62432974	test	0.9505	10.2025
JT4	129.61	126.6320541	2.97794593	test		
JT6	119.18	123.896958	−4.71695798	test		

4.4. FLAC^{3D} Numerical Simulation Result

The maximum surface subsidence was compared with the FZH during the advancement of the working face, as shown in Figure 12. When the face advanced to 100–400 m, both of these increased rapidly. As the face advanced to 400–500 m, the increase in the two was small. As the face advanced to 500–800 m, both the FZH and the maximum surface subsidence tended to be stable, only slightly increased. It can be seen that there was a certain correlation between the change curves of the two.

**Figure 12.** Relation between maximum surface subsidence and fracture height.

The data of horizontal stress and vertical stress from the stop line to the surface were extracted during the advancement of the working face. As can be seen from Figure 13, in the strata from the top of the coal seam up to 91 m, the characteristic changes in the horizontal stress were similar and were less affected by the advanced distance of the working face. From 91 m to 164 m from the top of the coal seam, the characteristic changes in horizontal stress showed differentiation. When the working face advanced greater than 400 m, the horizontal compression stress of the rock strata in this range fluctuated greatly, especially at places 115 m and 145 m away from the top of the coal seam, which also corresponded to the position where the height of the fractures changed significantly.

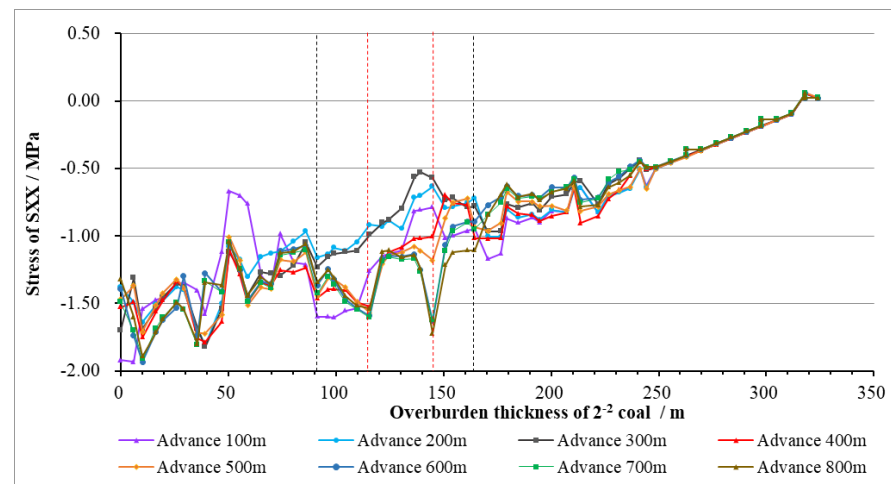


Figure 13. Contrast curve of horizontal stress.

The vertical stress characteristics can be seen in Figure 14. In the strata from the top of the coal seam up to 27 m, the characteristic changes in vertical compression stress were rapid reduction. The characteristic changes in vertical stress were differentiated from 27 m to 164 m from the top of the coal seam. When the working face advanced further than 400 m, the vertical stress of the rock strata in this range changed slowly, and the inflection point of stress change was about 99 m and 164 m away from the top of coal seam. There was also a significant correspondence with the change in the fracture height.

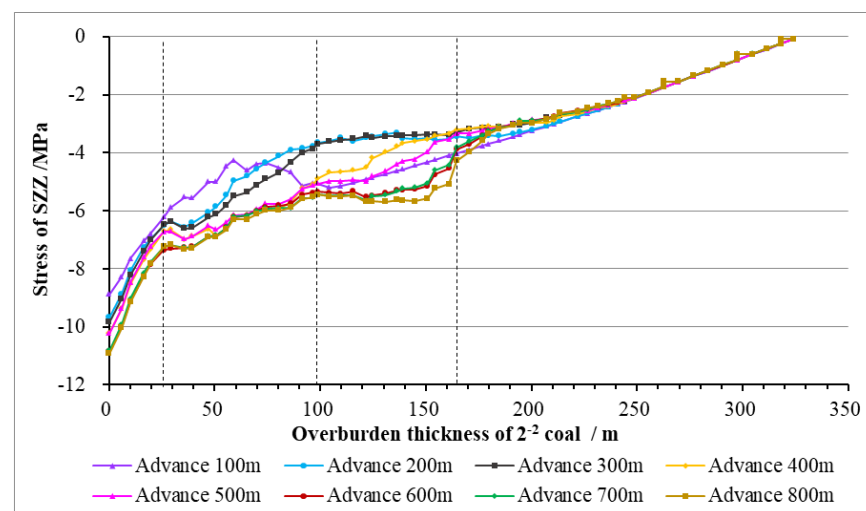


Figure 14. Contrast curve of vertical stress.

In conclusion, the surface subsidence is related to the FZH. When the height of the fracture increased suddenly, the horizontal stress and the vertical stress in the overburden vertically above the stop-mining line changed markedly.

5. Discussion

Firstly, the main discovery of this paper is the determination of the five factors influencing the maximum height of the fracture zone using a statistical analysis method based on the measured engineering data. Additionally, a model of the relationship between them and the maximum height of the fracture zone was established. Formulas (1) and (2) were given in the *Regulations of buildings, water, railway, and main well lane leaving coal pillar and press coal mining*, which were issued by the National Coal Mine Safety Administration of China. Formula (3) was proposed in the *Standard for exploration and evaluation of hydrogeol-*

ogy, engineering geology, and environment geology in coal beds (MT/T 1091-2008). This model is different from the empirical formulas stipulated in the Regulations and Standard as follows: The empirical formulas in the Regulations are qualitatively classified when the strength and hardness of rocks are involved, and different empirical formulas are given for different classifications. In this paper, the weighted average compressive strength of the Yan'an Formation and the Zhiluo Formation was calculated using the weighted calculation method according to the thickness ratio of different lithologies in the formation. Further, the empirical formula in the Regulations and Standard involved only one influencing factor, mining thickness, while this model considers five influencing factors. The empirical formulae given in the Regulations and Standard are not applicable to current high-intensity mining conditions [35]. Furthermore, Zhang et al. [17] established a prediction formula for FZH, including three influencing factors, as shown in Formula. However, due to the differences in the geological and mining characteristics of the sampling points used for obtaining the formula, the calculated results are quite different from the measured data.

$$H = \frac{100 \sum M}{1.6 \sum M + 3.6} \pm 5.6 \quad (6)$$

$$H = 20\sqrt{\sum M} + 10 \quad (7)$$

$$H = \frac{100M}{3.3n + 3.8} + 5.1 \quad (8)$$

$$H = 4.82M + 60.13 \ln \frac{s}{100} + 3.43M \ln \frac{b}{100} + 16.17 \quad (9)$$

where M is the mining thickness, s is the mining depth, b is the working face width, and n is the number of layers in the slice mining.

Figure 15 shows the calculated results of the empirical formulas and BPNN model, as well as the measured data. The results show that the predicted value of the BPNN model is closer to the measured value, while the predicted value of the empirical formula is smaller than the measured value.

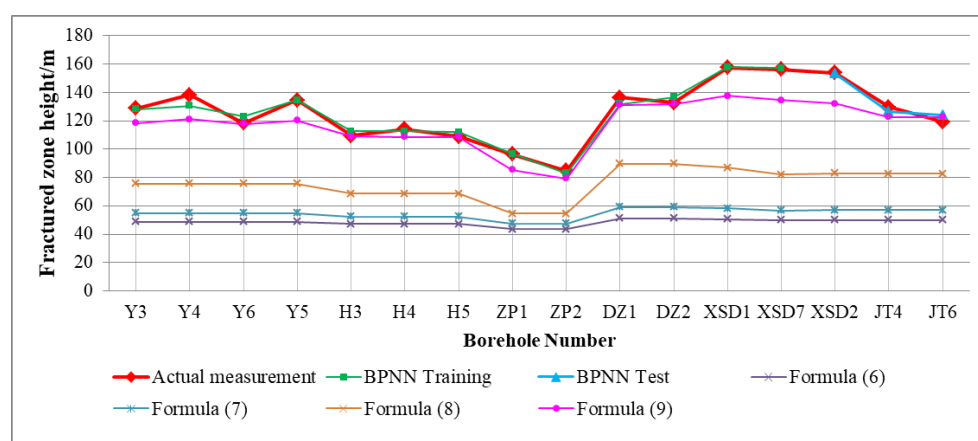


Figure 15. Comparison of values predicted by empirical formula and the measured values.

Secondly, in this paper, the mining thickness, mining depth, working face width, mining velocity, and the compressive strength of the overburden were taken into consideration as the influencing factors, and machine learning was used to study their degree of influence on the fracture zone. It was found that the mining thickness, mining depth, mining velocity, and the working face width promote the development of the fracture zone, while the compressive strength of the overburden inhibits the development of the fracture zone. Based on the key stratum theory and the mechanical analysis of overburden, Sun [36] described the movement and damage of the inner burden using the Analogous

Hyperbola Subsidence Model but did not study the relationship between the fracture zone and surface subsidence.

The FLAC^{3D} numerical simulation experiment was adopted to study the correlation between the fracture zone, surface subsidence, and stress concentration. According to the results of the FLAC^{3D} numerical simulation experiment, the fracture height changes synchronized with the surface subsidence amplitude, which is illustrated in Figure 12. At the same time, when the FZH and the surface subsidence change abruptly, this is also the position where the horizontal stress and the vertical stress change significantly, as shown in Figures 13 and 14. This phenomenon further indicates that the more focused the stress is, the more serious the strata fracture and the greater the surface subsidence will be. This method can be applied to mining damage studies anywhere. There are many parameters affecting rock strata movement and deformation, which are very complicated processes.

In fact, the mining of all mineral resources will destroy the original stress balance of the stratum, thus inducing rock strata movement and surface deformation. For example, groundwater exploitation in Xi'an resulted in the development of ground fissures [37]. Therefore, it is necessary to carefully consider the damage caused to the geological environment by the exploitation of mineral resources and to strengthen the research on this phenomenon.

6. Conclusions and Future Works

Firstly, in this study, the detection of FZH, the sample testing of rock mechanical properties, and the field monitoring of surface settlement were completed at Xiaobaodang Mine in the Yushen Mining Area of Jurassic Coal field in northern Shaanxi Province, China. The average mining thickness of the 112201 working face in Xiaobaodang No. 1 mine is 5.8 m, and the maximum height of the fractured zone is 157.46 m. The surface subsidence range increases as the distance of the face rise. The maximum subsidence is 3715 mm, which occurs along the center line of the working face strike.

Additionally, machine learning was used to determine the main factors influencing the maximum height of the fractured zone in the overburden and to establish a prediction model. These factors include mining thickness, mining depth, working face width, mining velocity, and the compressive strength of the overlying rock. The mining thickness, mining velocity, mining depth, and working face width are positively correlated with the FZH, while the uniaxial compressive strength of the overburden is negatively correlated with the FZH. There is a very complex nonlinear relationship between the influencing factors and the FZH. The fitting goodness (R^2) of the BPNN model can reach 97.22%, meaning that it is an effective method with which to predict the FZH.

Finally, the stress–strain law of roof strata in the process of coal mining was revealed by the FLAC^{3D} numerical simulation experiment, and the corresponding relationship between the FZH and surface subsidence was analyzed. During the mining process, the fracture zone develops rapidly where the stress changes significantly above the goaf, and the FZH is positively correlated with the extent of surface subsidence.

The spatial relationship between coal mining and mining damage was analyzed in this paper. The temporal relationship between rock strata movement and surface settlement after coal mining needs to be focused on in future work. Determining the quantitative relationship between the FZH and the surface subsidence is another one of our goals for further research.

Author Contributions: Conceptualization, L.M.; methodology, L.M., R.D. and X.S.; validation, Z.D. and Y.X.; formal analysis, L.M. and Y.X.; data curation, T.L. and L.M.; writing—original draft preparation, L.M.; writing—review & editing, R.D., X.S. and T.L.; supervision, Z.D. and Y.X.; project administration, Z.D. and L.M.; funding acquisition, L.M. and Z.D. All authors have read and agreed to the published version of the manuscript.

Funding: This research was funded by the Key Major Scientific Research Projects of Key Laboratory of Coal Resources Exploration and Comprehensive Utilization, Ministry of Natural Resources, China,

grant number No. MTDZ-ZD-2018-01. Innovation Project Foundation of Shaanxi Province, program No. 2018PT-23.

Data Availability Statement: Not applicable.

Acknowledgments: We thank the Key Laboratory of Coal Resources Exploration and Comprehensive Utilization, Ministry of Natural Resources, China and Innovation Project Foundation of Shaanxi Province for its support of this study. We thank the academic editors and anonymous reviewers for their kind suggestions and valuable comments. We thank Shaanxi 185 Coal Field Geology Co., Ltd. for engineering detection.

Conflicts of Interest: The authors declare no conflict of interest.

References

1. Jia, Z.J.; Wen, S.Y.; Sun, Z. Current relationship between coal consumption and the economic development and China's future carbon mitigation policies. *Energy Policy* **2022**, *162*, 112812. [\[CrossRef\]](#)
2. Zhang, Y.; Cao, S.G.; Zhang, N.; Zhao, C.Z. The application of short-wall block back fill mining to preserve surface water resources in northwest China. *J. Clean. Prod.* **2020**, *261*, 121232. [\[CrossRef\]](#)
3. Cui, Z.H.; Zhang, J.J.; Wu, D.; Cai, X.J.; Wang, H.; Zhang, W.S.; Chen, J.J. Hybrid many-objective particle swarm optimization algorithm for green coal production problem. *Inform. Sci.* **2020**, *518*, 256–271. [\[CrossRef\]](#)
4. Liu, Z.G.; Fan, Z.L.; Zhang, Y.J. Fracture characteristics of overlying bedrock and clay aquiclude subjected to shallow coal seam mining. *Mine Water Environ.* **2019**, *38*, 136–147. [\[CrossRef\]](#)
5. Jiang, S.Y.; Fan, G.W. Effect of mining parameters on surface deformation and coal pillar stability under customized shortwall mining of deep extra-thick coal seams. *Energy Rep.* **2021**, *7*, 2138–2154. [\[CrossRef\]](#)
6. Malinowska, A.; Hejmanowski, R. Building damage risk assessment on mining terrains in Poland with GIS application. *Int. J. Rock. Mech. Min. Sci.* **2010**, *47*, 238–245. [\[CrossRef\]](#)
7. Salmi, E.F.; Nazem, M.; Karakus, M. The effect of rock mass gradual deterioration on the mechanism of post-mining subsidence over shallow abandoned coal mines. *Int. J. Rock. Mech. Min. Sci.* **2017**, *91*, 59–71. [\[CrossRef\]](#)
8. Li, X.B.; Ji, D.L.; Han, P.H.; Li, Q.S.; Zhao, H.B.; He, F.L. Study of water-conducting fractured zone development law and assessment method in longwall mining of shallow coal seam. *Sci. Rep.* **2022**, *12*, 7994. [\[CrossRef\]](#)
9. Wan, L.M.; Hou, B.; Muhadasi, Y. Observing the effects of transition zone properties on fracture vertical propagation behavior for coal measure strata. *J. Struct. Geol.* **2019**, *126*, 69–82. [\[CrossRef\]](#)
10. Ning, J.G.; Wang, J.; Xu, Q. Mechanical mechanism of overlying strata breaking and development of fractured zone during close-distance coal seam group mining. *Int. J. Min. Sci. Technol.* **2020**, *30*, 207–215. [\[CrossRef\]](#)
11. Wang, Z.Q.; Li, J.K.; Qin, Z.C.; Su, Y.; Sidikovna, S.S. Height identification of water-permeable fractured zone based on synchronous movement in overlying strata. *Sci. Rep.* **2022**, *12*, 7592. [\[CrossRef\]](#) [\[PubMed\]](#)
12. Zhu, T.G.; Li, W.P.; Wang, Q.Q.; Hu, Y.B.; Fan, K.F.; Du, J.F. Study on the Height of the Mining-Induced Water-Conducting Fracture Zone Under the Q(2l) Loess Cover of the Jurassic Coal Seam in Northern Shaanxi, China. *Mine Water Environ.* **2020**, *39*, 57–67. [\[CrossRef\]](#)
13. Liu, X.S.; Fan, D.Y.; Tan, Y.L.; Ning, J.G.; Song, S.L.; Wang, H.L.; Li, X.B. New Detecting Method on the Connecting Fractured Zone above the Coal Face and a Case Study. *Rock. Mech. Rock. Eng.* **2021**, *54*, 4379–4391. [\[CrossRef\]](#)
14. Tan, Y.; Guo, W.B.; Bai, E.H. The height of fractured zones caused by strip Wongawilli mining in a shallow buried coal seam underlying a hard roof. *Curr. Sci.* **2018**, *115*, 1387–1392. [\[CrossRef\]](#)
15. Guo, W.B.; Zhao, G.B.; Wang, S.R. Height of fractured zone inside overlying strata under high-intensity mining in China. *Int. J. Min. Sci. Technol.* **2019**, *29*, 45–49. [\[CrossRef\]](#)
16. Wu, F.Z.; Wang, Y.N.; Zhu, Z.Q. Height of interconnected fracture zone based on the impact of rock fragmentation and bulking. *Energ. Explor. Exploit.* **2021**, *39*, 869–885. [\[CrossRef\]](#)
17. Liu, Y.; Yuan, S.C.; Ye, Z.Y. Predicting the height of the water-conducting fractured zone using multiple regression analysis and GIS. *Environ. Earth. Sci.* **2019**, *78*, 422. [\[CrossRef\]](#)
18. Zhang, D.S.; Li, W.P.; Lai, X.P.; Fan, G.W.; Liu, W.Q. Development on basic theory of water protection during coal mining in northwest of China. *J. China Coal Soc.* **2017**, *42*, 36–43.
19. Fan, L.M.; Zhang, X.T.; Xiang, M.X.; Zhang, H.Q.; Shen, T. Characteristics of ground fissure development in high intensity mining area of shallow seam in Yushenfu coal field. *J. China Coal Soc.* **2015**, *40*, 1442–1447.
20. Fan, L.M.; Ma, X.D.; Li, Y.H.; Li, C.; Yao, C.W. Geological disasters and control technology in high intensity mining area of western China. *J. China Coal Soc.* **2017**, *42*, 276–285.
21. Li, J.; Wang, L. Mining subsidence monitoring model based on BPM-EKTF and TLS and its application in building mining damage assessment. *Environ. Earth Sci.* **2021**, *80*, 396. [\[CrossRef\]](#)
22. Chen, Q.J.; Li, J.Y.; Hou, E.K. Dynamic simulation for the process of mining subsidence based on cellular automata model. *Open Geosci.* **2020**, *12*, 832–839. [\[CrossRef\]](#)

23. Li, C.; Zhao, L.; Ding, L.; Li, M.; Wang, S.; Jia, P.; He, Y. *Collaborative Dynamic Prediction Method for Overlying Strata and Ground Subsidence Induced by Coal Mining, Involves Substituting Main Influence Radius and Subsidence Coefficient into Surface Subsidence under Influence of Mining*; Henan Polytechnic University: Jioazuo, China, 2020; p. A11950.
24. Gong, Y.Q.; Guo, G.L.; Wang, L.P.; Zhang, G.J.; Zhang, G.X.; Fang, Z. Numerical Study on the Surface Movement Regularity of Deep Mining Underlying the Super-Thick and Weak Cementation Overburden: A Case Study in Western China. *Sustainability* **2022**, *14*, 1855. [\[CrossRef\]](#)
25. Huang, Q.X.; He, Y.P.; Cao, J. Experimental investigation on crack development characteristics in shallow coal seam mining in China. *Energies* **2019**, *12*, 1302. [\[CrossRef\]](#)
26. Chen, M.; Yang, S.Q.; Ranjith, P.G.; Yuanchao Zhang, Y.C. Cracking behavior of rock containing non-persistent joints with various joints inclinations. *Theor. Appl. Fract. Mech.* **2020**, *109*, 102701. [\[CrossRef\]](#)
27. Chen, M.; Zang, C.W.; Ding, Z.W.; Zhou, G.L.; Jiang, B.Y.; Zhang, G.C.; Zhang, C.P. Effects of confining pressure on deformation failure behavior of jointed rock. *J. Cent. South. Univ.* **2022**, *29*, 1305–1319. [\[CrossRef\]](#)
28. Moradzadeh, A.; Mohammadi-Ivatloo, B. Heating and cooling loads forecasting for residential buildings based on hybrid machine learning applications: A comprehensive review and comparative analysis. *IEEE Access* **2022**, *10*, 2196–2215. [\[CrossRef\]](#)
29. Xu, H.T.; Chen, C.B.; Zheng, H.W.; Luo, G.P.; Yang, L.; Wang, W.S.; Wu, S.X. Correlation analysis and adaptive genetic algorithm based feature subset and model parameter optimization in salinization monitoring. *J. Geo-Inform. Sci.* **2020**, *22*, 1497–1509.
30. Zhang, J.G.; Li, P.T.; Yin, X.; Wang, S.; Zhu, Y.G. Back analysis of surrounding rock parameters in pingdingshan mine based on bp neural network integrated mind evolutionary algorithm. *Mathematics* **2022**, *10*, 1746. [\[CrossRef\]](#)
31. Zhang, H.; Gui, L.; Wang, T.F.; Yang, S. Prediction of quaternary cover thickness and 3D geological modeling based on bp neural network. *Earth Sci.* **2022**, 1–9. Available online: <https://kns.cnki.net/kcms/detail/detail.aspx?dbcode=CAPJ&dbname=CAPJLAST&filename=DQKX2022052500D&uniplatform=NZKPT&v=yvVLpZpX-NRs6NwZd8Gj08bOJrEyMSILP3ici3QbOVxyLX743cGibIS-7aiElg95> (accessed on 14 July 2022).
32. Bai, Y.F.; Li, X.J.; Lv, M.Y. Multiscale analysis of tunnel surrounding rock disturbance: A PFC^{3D}-FLAC^{3D} coupling algorithm with the overlapping domain method. *Comput. Geotech.* **2022**, *147*, 104752. [\[CrossRef\]](#)
33. Hu, X.J.; Li, W.P.; Cao, D.T.; Liu, M.C. Index of multiple factors and expected height of fully mechanized water flowing fractured zone. *J. China Coal Soc.* **2012**, *37*, 613–620.
34. Li, Y.; Yang, T.H.; Hao, N. Mining rate effect of high-intensity working face based on stress release rate and microseismic monitoring. *J. Min. Saf. Eng.* **2021**, *38*, 295–303.
35. Dai, S.; Han, B.; Liu, S.L.; Li, N.B.; Geng, F.; Hou, X.H. Neural network-based prediction methods for height of water-flowing fractured zone caused by underground coal mining. *Arab. J. Geosci.* **2020**, *13*, 495. [\[CrossRef\]](#)
36. Sun, Y.J.; Zuo, J.P.; Karakusb, M.; Wang, J.T. Investigation of movement and damage of integral overburden during shallow coal seam mining. *Int. J. Rock Mech. Min.* **2018**, *117*, 63–75. [\[CrossRef\]](#)
37. Peng, J.B.; Chen, L.W.; Huang, Q.B.; Men, Y.M.; Fan, W.; Yan, J.K.; Li, K.; Ji, Y.S.; Shi, Y.L. Large-scale physical simulative experiment on ground-fissure expansion mechanism. *Chin. J. Geophys.* **2008**, *51*, 1826–1834.